

# In Vivo Syngeneic Tumor Models with Acquired Resistance to Anti-PD-1/PD-L1 Therapies

Morgane Denis<sup>1,2</sup>, Chloé Grasselly<sup>1,2</sup>, Pierre-Antoine Choffour<sup>2</sup>, Anne Wierinckx<sup>1</sup>, Doriane Mathé<sup>2</sup>, Kamel Chettab<sup>1</sup>, Anne Tourette<sup>2</sup>, Nolan Talhi<sup>2</sup>, Aurore Bourguignon<sup>1</sup>, Fabian Birzele<sup>3</sup>, Elsa Kress<sup>2</sup>, Lars Petter Jordheim<sup>1</sup>, Christian Klein<sup>4</sup>, Eva-Laure Matera<sup>1</sup>, and Charles Dumontet<sup>1,5</sup>



## ABSTRACT

Antibodies targeting PD-1 and PD-L1 have produced durable responses in a subset of patients with cancer. However, a majority of these patients will ultimately relapse due to acquired resistance. To explore the underlying mechanisms of this secondary resistance, we developed five syngeneic murine tumor variants with acquired resistance to anti-PD-1 and/or PD-L1 antibodies *in vivo*. Resistant *in vivo* models were obtained by serial treatment/reimplantation cycles of the MC38 colorectal, MB49 and MBT2 bladder, and RENCA kidney and TyrNras melanoma models. Tumor immune infiltrates were characterized for wild type and resistant tumors using spectral cytometry and their molecular alterations analyzed using RNA sequencing analyses. Alterations in the tumor immune microenvironment were strongly heterogeneous among resistant models, involving select lymphoid and/or myeloid subpopulations.

Molecular alterations in resistant models included previously identified pathways as well as novel candidate genes found to be deregulated in several resistant models. Among these, *Serpinf1*, coding for pigment epithelial-derived factor (PEDF) was further explored in the MC38 and the MBT2 models. Overexpression of *Serpinf1* induced resistance to anti-PD-1 antibodies in the MC38 model, whereas knockdown of *Serpinf1* sensitized this model as well as the primarily resistant MBT2 model. *Serpinf1* overexpression was associated with increased production of free fatty acids and reduced activation of CD8<sup>+</sup> cells, while orlistat, a compound that reduces the production of free fatty acids, reversed resistance to anti-PD-1 therapy. Our results suggest that a panel of syngeneic resistant models constitutes a useful tool to model the heterogeneity of resistance mechanisms encountered in the clinic.

## Introduction

Immune checkpoint inhibitors (ICI) directed against programmed cell death 1 (PD-1) and programmed cell death ligand 1 (PD-L1) have shown impressive clinical efficacy in a wide range of cancer types. Several mAbs have been approved by the FDA for the treatment of patients with various indications including melanoma, non-small cell lung cancer (NSCLC), bladder cancer, and renal cell carcinoma (1–4). mAbs targeting PD-1 and PD-L1 allow the restoration of T-cell antitumor functions (5). However, a large proportion of patients demonstrates *de novo* resistance to these therapies or relapse after a primary response.

Mechanisms of resistance to ICIs remain poorly understood. Mutations inducing  $\beta$ -catenin activation have been linked to primary resistance to anti-PD-L1 and anti-CTLA-4 treatment, correlating with T-cell evasion in patients with melanoma (6). Mutations in  $\beta$ 2 microglobulin causing inefficient antigen presentation by HLA class

1, as well as mutations of Janus kinase 1 (JAK1) and Janus kinase 2 (JAK2) genes causing a loss of IFN response, have been associated with acquired resistance to PD-1-targeting agents in patients with melanoma (7). Using a genetically engineered mouse model of lung cancer, Koyama and colleagues showed an upregulation of the alternative immune checkpoint T-cell immunoglobulin and mucin-domain containing-3 (TIM-3) in infiltrating T cells associated with acquired resistance to anti-PD-1 blockade (8). Overall, these data suggest that the underlying mechanisms of innate and acquired resistance are likely to be multifactorial and remain largely undetermined. Three main causes explaining why it is so challenging to study acquired resistance mechanisms have been identified: the absence of uniform terminology, the difficulty in obtaining patient tumor samples and the lack of a powerful tool to study such mechanisms (9). The establishment of robust *in vivo* variants derived from sensitive models is a promising means to decipher the mechanisms of acquired resistance to immune checkpoint antibodies, as they allow comparison with their sensitive parental counterparts. The mechanistic hypotheses generated from such models can subsequently be validated in the clinical setting. Moreover, these models are powerful tools to evaluate new treatments or therapeutic combinations for patients with acquired resistance to PD-1/PD-L1 antibodies.

In this study, we used immunocompetent mouse models to analyze diverse types of syngeneic mouse tumors (colorectal, bladder, renal, and melanoma cancers) chosen for their initial sensitivity to anti-PD-1/anti-PD-L1 axis blockade and developed *in vivo* resistant models. Because acquired resistance is defined by the emergence of reduced sensitivity to therapy after an initial response to this same agent, we chose to compare the characteristics of the resistant models at basal state with those of the corresponding sensitive models, focusing on differences in immune cell infiltrates and alterations in the transcriptional profiles. Modifications in the tumor immune infiltrate were further explored by testing combinations of alternative ICIs in an effort to reverse the resistant phenotype. Pooling of

<sup>1</sup>Univ Lyon, Université Claude Bernard Lyon 1, INSERM 1052, CNRS 5286, Centre Léon Bérard, Centre de Recherche en Cancérologie de Lyon, Lyon, France.

<sup>2</sup>Antineo, Lyon, France. <sup>3</sup>Roche Pharma Research & Early Development, Pharmaceutical Sciences, Roche Innovation Center Basel, Basel, Switzerland.

<sup>4</sup>Roche Pharma Research & Early Development, Roche Innovation Center Zurich, Schlieren, Switzerland. <sup>5</sup>Hospices Civils de Lyon, Lyon, France.

**Note:** Supplementary data for this article are available at Cancer Immunology Research Online (<http://cancerimmunolres.aacrjournals.org/>).

M. Denis and C. Grasselly contributed equally to this article.

**Corresponding Author:** Charles Dumontet, INSERM 1052/CNRS 5286/University of Lyon, 8 Avenue Rockefeller, Lyon 69008, France. E-mail: [charles.dumontet@chu-lyon.fr](mailto:charles.dumontet@chu-lyon.fr)

Cancer Immunol Res 2022;XX:XX-XX

doi: 10.1158/2326-6066.CIR-21-0802

©2022 American Association for Cancer Research

molecular analyses allowed us to identify altered expression of genes potentially related to resistance mechanisms in several of our resistant tumor models.

We chose to focus on *Serpinf1*, which codes for a serine proteinase inhibitor, pigment epithelium-derived factor (PEDF; ref. 10). PEDF is a multifunctional protein with neuroprotective, antiangiogenic, and lipid metabolic properties (10, 11). Although some studies have shown that proliferation and migration are inhibited in presence of PEDF in melanoma (12), other investigators have demonstrated an opposite effect in esophageal squamous cell carcinoma (13). It has also been suggested that PEDF may enhance the suppressive phenotype of regulatory T cells (Treg) (14). The impact of PEDF on tumor growth may depend on its location. Secretion of PEDF in the extracellular compartment may have a direct antitumoral role through antiangiogenic effects, whereas intracellular PEDF may have a protumoral role through free fatty acid (FFA) accumulation (15).

PEDF has been shown to be involved in lipid metabolism, as it binds to and activates adipose triglyceride lipase (ATGL), a protein that catalyzes the first hydrolysis reaction of triacylglycerols (11). There is growing evidence that a lipid-rich tumor microenvironment may favor immunosuppressive populations. Of note, PD-1/PD-L1 binding promotes lipolysis and fatty acid oxidation (FAO), whereas anti-PD-1 treatment favored metabolic reprogramming of T cells with activation of glycolytic pathways (16). However, if the balance tilts in favor of lipid rather than carbohydrate metabolism, T cells may shift to exhausted and regulatory phenotypes (17, 18). We therefore sought to determine whether the overexpression of *Serpinf1* observed in some of our resistant models was involved in the increased lipid load observed in these tumors. Our results suggest that increased expression of *Serpinf1* is associated with alterations in FFA metabolic pathways which may be involved in resistance to anti-PD-1 therapy.

## Materials and Methods

### Mouse cell line cultures

MC38 and RENCA cell lines were obtained from Kerastat (CVCL\_B288) and ATCC (CRL-2947), respectively. Alain Bergeron (Laval University, Québec, Canada) provided the MB49 and MBT2 cell lines, Julie Caramel (CRCL, France) provided the TyrNras cell line, and Emmanuel Bachy (HCL) provided the HEK293T cell line. We received all cell lines between 2016 and 2021. Cell lines were reauthenticated between 2020 and 2022 by genotyping (Microsynth). All cell lines were negative for *Mycoplasma* assays. Murine colon cancer MC38 cells and HEK293T cells were cultured in DMEM (Gibco, 41966-029) with 10% FBS (Gibco, A3160802) and 100 U/mL penicillin and streptomycin (Gibco, 15140122). The murine renal cell carcinoma cell line RENCA, the melanoma cell line TyrNras, and the murine bladder cancer cell lines MBT2 and MB49 were cultured with RPMI medium (Gibco, 21875-034) with 10% FBS (Gibco, A3160802) and 100 U/mL penicillin and streptomycin (Gibco, 15140122). Cell lines were thawed and directly amplified for *in vivo* experiments. Cells were incubated in a humidified incubator with 5% CO<sub>2</sub> at 37°C.

### Establishment of resistant models

MC38 cells, MB49 cells, and TyrNras cells were injected in 4–5 weeks old female C57BL6 mice (Charles River Laboratory, 000664), RENCA cells were injected in 4 to 5 weeks old female BALB/c mice (Charles River Laboratory, 000651), and MBT2 cells were injected in 4 to 5 weeks old female C3H/HeNRj mice (Janvier Laboratory). In all cases,  $5 \times 10^6$  cells of exponentially growing cultures were diluted in

0.2 mL of PBS (Gibco, 140040-091) and injected subcutaneously into the left flank. The tumor volume was measured twice a week (length  $\times$  width) with a caliper. The tumor volume was determined using the formula:  $4/3 \times \pi \times r^3$ . When the tumor volume reached 150 mm<sup>3</sup>, that is, between 7 and 15 days according to tumor growth, mice were randomized and the first treatment was administered to groups of 5–6 mice for tumor growth and flow cytometry analyses. To establish the resistant models, tumors obtained from mice with initial responses to anti-PD-1 (BioXCell, RMP1-14, BE014, RRID: AB\_10949053, 12.5 mg/kg/week, i.p.) or anti-PD-L1 (BioXCell, 10F.9G2, BE0101, RRID: AB\_10949073, 12.5 mg/kg/week, i.p.; Fig. 1A), were serially reimplanted subcutaneously into new groups of naive mice and treated once a week to maintain selection pressure. At each passage, three naïve mice were implanted with tumor fragments and treatment was initiated once the tumor reached 150 mm<sup>3</sup>. The most aggressive tumor was selected for reimplantation. At least five passages were necessary to induce acquired resistance (Fig. 1A). We will refer to sensitive models as wild type (WT) and to resistant models as anti-PD-1-R or anti-PD-L1-R for those resistant to anti-PD-1 and anti-PD-L1 mAbs, respectively. All resistant models were frozen to constitute stocks. The resistant models were regularly tested for resistance to anti-PD-1 or anti-PD-L1 and demonstrated a stable phenotype. All mice were raised in an specific pathogen-free environment with free access to standard food and water. Experimental procedures were submitted and approved by the Animal Ethics Committee CECCAP of Lyon. We used the ARRIVE guidelines when writing our animal experimental protocol (19).

### Flow cytometry analysis

Baseline immunophenotyping was performed in all models when the tumor volume reached approximately 200 mm<sup>3</sup>, acquired on a Cytek Aurora flow cytometer with SpectroFloSoftware (Cytek Biosciences). For all MC38 models, a complementary flow cytometry experiment was performed 24 hours after the second treatment, and samples were acquired on the FortessaX20 flow cytometer with BD FACS Diva software (BD Biosciences). For all experiments, mouse tumor dissociation kits (Miltenyi Biotec, 130-096-730) were used. To digest tumors, we used the gentle MACS Octo Dissociator (Miltenyi Biotec, 130-096-427). After filtration through a 100  $\mu$ m filter (Miltenyi Biotec, 130-110-917) and wash with PBS, cells were stained with a viability dye marker and blocked with anti-CD16/32 (BioLegend, 101320) according to the manufacturer's instructions. Cells were stained with the fluorescently labeled antibodies in the dark for 30 minutes at 4°C. After surface staining, cells were fixed and permeabilized using BD Cytofix/Cytoperm kit (BD, 554714), then labeled with F4/80, FoxP3, granzyme B, CD206 and/or T-bet in the dark for 30 minutes at 4°C. FlowJo software (BD) was used for analyses and GraphPad Prism software was used for statistical analysis (ANOVA with Bonferroni post-hoc test). Antibodies and gating strategies are described in Supplementary Tables S1 and S2, respectively.

### RNA sequencing

Because of availability at different periods, RNA sequencing (RNA-seq) was performed on two separate platforms. WT, anti-PD-1-R, anti-PD-L1-R MB49 tumors; WT, anti-PD-1-R, anti-PD-L1-R TyrNras tumors; and WT, anti-PD-L1-R MC38 tumors were processed by the ProfileXpert platform with samples of 200 mm<sup>3</sup>. After grinding of samples, RNA was extracted using RNeasy mini kit (Qiagen, catalog no. 74104). Quality of samples was checked by Bioanalyzer 2100 (Agilent) and RNA was quantified by Nanodrop. Thereafter, 5  $\mu$ g of RNA was enriched by NextFlex Rapid Directional

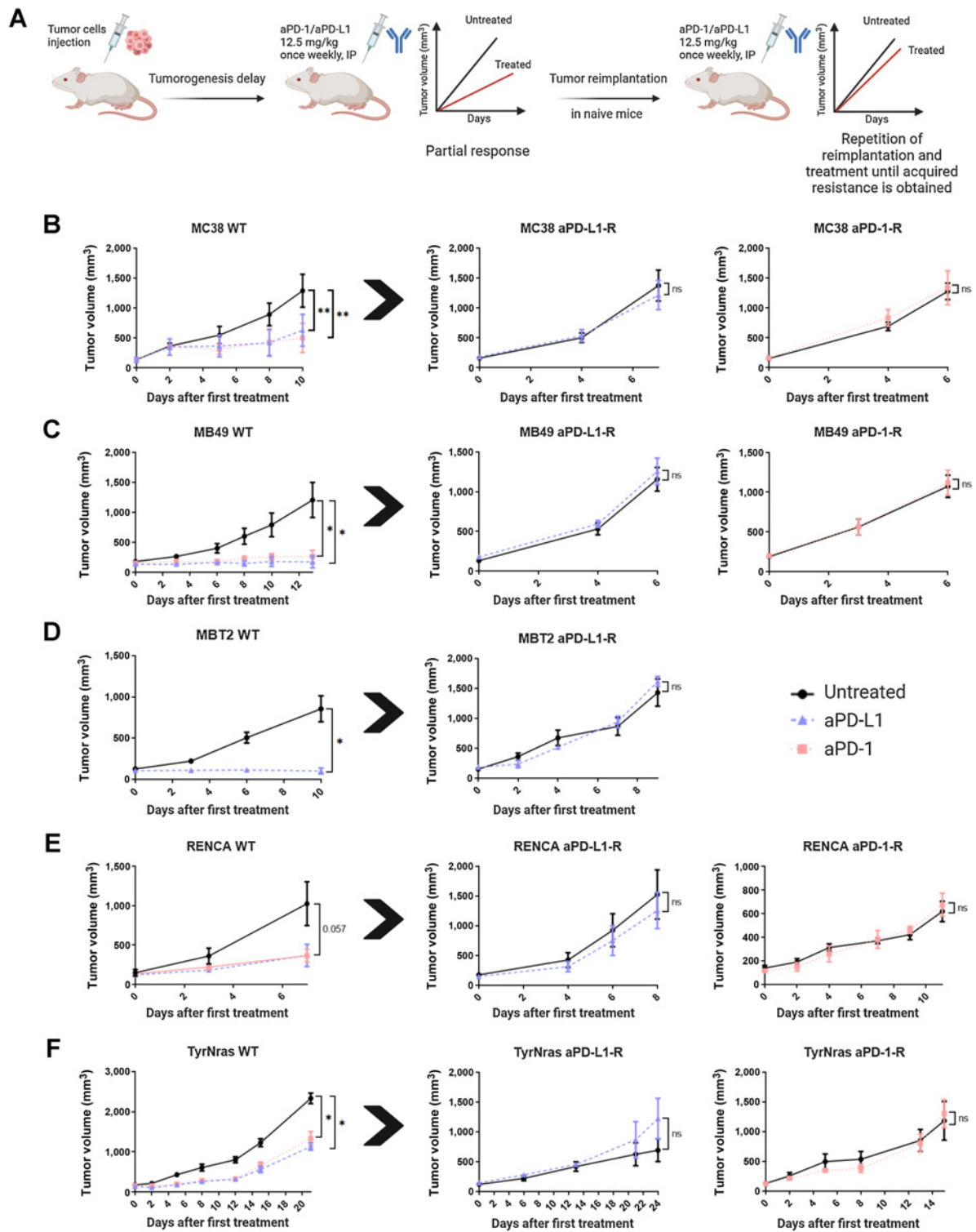


**Figure 1.**

WT sensitive models were rendered resistant to anti-PD-1 and/or anti-PD-L1 *in vivo*. **A**, Tumor cell lines were injected in mice to establish the resistant models and treated with anti-PD-1 or anti-PD-L1. Fragments of tumors displaying a primary response to anti-PD-1 or anti-PD-L1 were then implanted subcutaneously into new groups of tumor-naïve mice and treated once a week to maintain selection pressure. At least five passages were necessary to induce acquired resistance. **B-F**, Mean tumor volume for MC38 colorectal cancer (**B**), MB49 bladder cancer (**C**), MBT2 bladder cancer (**D**), RENCA kidney cancer (**E**), and TyrNras melanoma cancer (**F**). Error bars are  $\pm$  SEM.  $n = 4$  or 6 mice/group; ns, not significant; \*,  $P < 0.05$  and \*\*,  $P < 0.01$ , using Mann-Whitney  $t$  test.

mRNA-seq kit (Bio-Scientific). Quality of samples was verified again by Bioanalyzer 2100 (Agilent) and quantified by qPCR with KAPA Library Quantification Kit for Illumina (Roche). Samples were put on Flow Cell High Output. Amplification and sequencing were performed with Illumina NextSeq500: run Single Read 75 bp was performed for MC38 and TyrNras models and paired-end 2 × 75 cycles for MB49 models. For WT and anti-PD-1-R MC38 tumors, WT and anti-PD-L1-R MBT-2 tumors, and WT, anti-PD-1-R and anti-PD-L1-R RENCA tumors, the RNA-seq was performed by Roche, with samples of 200 mm<sup>3</sup>. The Qiagen Tissue Lyser together with the RNeasy Mini Kit (Qiagen, catalog no. 74104) was used to extract RNA from tissue. Samples were randomized before sequencing library preparation and sequencing. Extracted RNA was of high quality (RNA integrity number, 7.8–10) and 500 ng (as quantified using Agilent Bioanalyzer) of extracted total RNA was used for whole mRNA-seq library preparation. The protocol for Illumina TruSeq stranded mRNA library preparation (Illumina, catalog no. RS-122-2101) was followed. The yield and quality of RNA-seq libraries was assessed on the Agilent Bioanalyzer. Libraries were sequenced on the Illumina HiSeq4000 system, paired-end 2 × 51 cycles.

All RNA-seq samples passed quality control in terms of number of reads per sample and read quality (Q30 >90% along the full read length and full read coverage of expressed genes and transcripts). For samples treated by ProfileXpert platform, trimming of single reads was performed using cutadapt v1.9.1 software. Then the reads were mapped using Tophat2 v2.1.1 software with default parameters on the genome *Mus musculus* GRCm38/mm10. Alignment rates to the mouse genome were above 95%. The fragments per kilobases of exon per million mapped reads values were then computed for each gene using Cufflinks v2.1.1 software as described by Trapnell and colleagues (20). For samples treated by Roche platform, paired-end reads were aligned to the mouse genome (NCBIM37.67) using gsnap (21). Alignment rates to the mouse genome were above 80%. The reads per kilobase of transcript per million mapped reads values were then computed for each gene as described by Mortazavi and colleagues (2008) using the gene composite length, that is, the sum of the length of all nonoverlapping exon groups as normalization factor, using in-house tools implemented in Java (22). Differential gene expression between WT and resistant models were computed using R scripts with limma package version 3.46.0 for a fold change ≥ 1 and the *P* value > 0.05 (23). The canonical pathways were generated using ingenuity pathway analysis (QIAGEN Inc: <https://www.qiagenbioinformatics.com/products/ingenuitypathway-analysis>). Pathways significantly predicted to be upregulated or downregulated (*z* score ± 1.5 and *P* < 0.05) for each models are recapitulated in Supplementary Table S3. Differential gene expression between WT and resistant models were processing with fold change ≥ 1 and the *P* > 0.05. Venn diagrams were performed (24). For heat map representation, we used package on R software pheatmap (<https://cran.r-project.org/web/packages/pheatmap/index.html>).

#### Evaluation of therapeutic combinations in resistant models

MB49 anti-PD-1-R, MC38 anti-PD-1-R, and MC38 anti-PD-L1-R tumor fragments were implanted subcutaneously into the left flank of immunocompetent C57Bl/6 mice. RENCA anti-PD-1-R tumor fragments were implanted subcutaneously into the left flank of immunocompetent BALB/C mice. When tumor volumes reached 150 mm<sup>3</sup>, mice were randomized and the first treatment was administered (4 to 6 mice per group). Untreated groups received IgG2a as a control (BioXCell, clone 2A3, BE0089, RRID: AB\_1107769, 12.5 mg/kg/week,

i.p.). In the MC38 anti-PD-1-R model, we tested four combinations with anti-PD-1 treatment: (i) anti-TNFα (BioXCell, clone XT3.11, BE0058, RRID: AB\_1107764, 10 mg/kg/week, i.p.), (ii) anti-CD47 (BioXCell, clone MIAP301, BE0270, RRID: AB\_2687793, 20 mg/kg twice a week, i.p.), (iii) anti-Ly6G (BioXCell, clone 1A8, BP0075-1, RRID: AB\_1107721, 2.5 mg/kg once daily, i.p.), and (iv) orlistat (Roche, 240 mg/kg/day, i.p.) with anti-PD-1 (BioXCell, RMP1-14, 12.5 mg/kg/week, i.p.). We also combined anti-CSF1R (BioXCell, clone AFS98, BE0213, RRID: AB\_2687699, 20 mg/kg one day after anti-PD-1 then every 2 days) with anti-PD-1 in the MB49 anti-PD-1-R model. Finally, we combined anti-CD25 (BioXCell, clone PC-615.3, BE0012, RRID: AB\_1107619, 20 μg/kg) with anti-PD-L1 to treat MC38 anti-PD-L1-R bearing mice. For RENCA anti-PD-1-R model, we combined anti-TIM-3 (BioXCell, clone RMT3-23, BE0115, RRID: AB\_10949464, 12.5 mg/kg twice a week), anti-LAG-3 (BioXCell, clone C9B7W, BE0174, RRID: AB\_10949602, 10 mg/kg twice a week) or anti-CTLA-4 (BioXCell, clone 9D9, BE0131, RRID: AB\_10950184, 5 mg/kg twice a week) with anti-PD-1.

#### Modification of candidate gene expression

*Serpinf1* knockout MC38 cells and MBT2 cells were generated using CRISPR/Cas9 technology. Oligonucleotides were inserted into pLentiCRISPRv2-puro plasmid (Addgene) using BsmBI (Thermo Fisher Scientific-Fermentas). Targeting and control sequences are as follows:

KO *Serpinf1*-F: CAGTCCAGAGGAGTAGCACCGTTTT  
 KO *Serpinf1*-R: GGTGCTACTCCTCTGGACT  
 KO Non target Control-F: AACGGTAGCGTACCCGTGAA  
 KO Non target Control-R: TTCACGGGTACGCTACCGTT

Virus particles were produced using HEK 293T cells. After 24 hours incubation, medium was changed and supernatant collected twice with 24 hours intervals. Supernatant was filtered using 0.45 μm filter. MC38 and MBT2 (60% confluency) were incubated in lentivirus-containing medium with polybrene (10 μg/mL; Sigma-Aldrich, H9268-10G) for 6 hours. After 48 hours following infection, puromycin (Sigma-Aldrich, P9620) was added at 2.5 and 4 μg/mL, respectively.

To obtain MC38 variants with stable overexpression of the candidate gene, cells were transfected with pcDNA3.1+ plasmid containing cDNAs of *Serpinf1* sequence (Thermo Fisher Scientific). At day 1, cells were added to obtain 70% of confluence in Falcon T25 flask. A total of 5 μg of corresponding pcDNA3.1+ plasmid was added with lipofectamine (Invitrogen, 11668030) for six hours. On day 4, geneticin (Life Technologies, 10131-027) at 1 mg/mL concentration was used to select transfected MC38 cells. Empty plasmid was used as negative control.

#### Immunohistochemistry

After fixation, MC38 and MBT2 WT and variant tumors were dehydrated and impregnated in the LEICA ASP300 machine. After inclusion, samples were cut to 3 μmol/L and mounted on a Superfrost+ slide (Eprelia, J1800AMNZ). Roche DAB Map Kit (Roche, 760-124) was used on a Roche Discovery XT machine. After unmasking with a buffer, PEDF (R&D, AF1149), ATGL (Cell Signaling Technology, 2138), CD8a (Invitrogen, 14-0808-82) antibodies were diluted at 1/500, 1/200, and 1/200, respectively, and incubated 60 minutes at 37°C. Slides were then incubated with secondary antibody 32 minutes at 37°C. For PEDF, we used rabbit Anti-Goat IgG Biotinylated Antibody (Vector, BA5000) at 1/300, and for ATGL and CD8a, we used rabbit Anti-Rat IgG Biotinylated Antibody (Vector, BA4001) at 1/100 and 1/200, respectively. To explore lipid content, Oil Red O (ORO; Diapath, C0512) solution was added for 15 minutes after fixation with isopropanol 60%. Slides were rinsed with isopropanol

60% and water. Harris hematoxyline was added for 1 minute and slides were rinsed with water. Zeiss ZEN blue edition software was used to obtain representative images.

### Lipid extraction and analyses of FFAs

Mouse tumors were crushed and weighed. After the addition of appropriate internal standards, total lipids were extracted twice with ethanol/chloroform [1:2, volume for volume (v/v)]. The organic phases were dried under nitrogen. Lipid classes were then separated by solid phase extracted [NH<sub>2</sub> 3CC (500MG)]. Total lipids were placed on aminopropyl columns, previously activated with 8 mL of hexane (Merck, 1.04369.2500). Each lipid class was eluted using a different solvent: 20 mL chloroform (VWR, 22711.290) for neutral lipids and 5 mL diethyl ether/acetic acid (Carlo Erba, P0441016 and 401422, respectively; 98:2, v/v) for FFA. The FFA fraction was dried under nitrogen and derived with boron trifluoride in methanol (14%; Sigma, B1252). Transmethylation was carried out at 100°C in screw-capped tubes for 1 hour. The derivatized fatty acid methyl esters were then extracted twice with isooctane (Merck, 1.15440.1000) and analyzed by gas chromatography using an HP6890 instrument equipped with a fused silica capillary BPX70 SGE column (60 × 0.25 mm). The vector gas was hydrogen. Temperatures of the flame ionization detector and the split/splitless injector were set at 250°C and 230°C, respectively.

### Availability of data and material

The authors declare that data and Supplementary Data files supporting the findings of this study are available. Further information and requests for resources and reagents should be directed to the lead contact, Charles Dumontet (charles.dumontet@chu-lyon.fr). *In vivo* models will be made freely available to other investigators. RNA-seq data are available with the bioproject accession number PRJNA637469 (<https://www.ncbi.nlm.nih.gov/sra/PRJNA637469>).

### Ethics approval and consent to participate

Experiments using C57Bl/6, C3H, or BALB/C mice were submitted to and approved by the Animal Ethics Committee CECCAP of Lyon.

## Results

### Development of models with *in vivo* resistance to anti-PD-1 and anti-PD-L1

First, we identified five murine cell line models, which were robustly sensitive to treatment with PD-1 and/or PD-L1 mAbs. All WT models were sensitive to both PD-1 and PD-L1 blockade, except for MBT-2, which was sensitive to PD-L1 blockade only. We established nine resistant models, five selected with PD-L1 mAb and four with PD-1 mAb, with treatment regimens that induced partial response in all of these models and consisted of anti-PD-1 or anti-PD-L1 treatment (12.5 mg/kg), initiated when tumor volume reached 150 mm<sup>3</sup>, administered intraperitoneally (i.p.) once per week. These models had become resistant to the selecting agent after five serial implantations and exposure to antibodies (Fig. 1A). Models included the colorectal cancer MC38 model (Fig. 1B; Supplementary Fig. S1A), two bladder cancer models MB49 (Fig. 1C; Supplementary Fig. S1B) and MBT-2 (Fig. 1D; Supplementary Fig. S1C), the renal cell carcinoma RENCA (Fig. 1E; Supplementary Fig. S1D), and a melanoma TyrNras models (Fig. 1F; Supplementary Fig. S1E).

Once these models had been established, we evaluated their cross-resistance to the other ICI targeting the anti-PD-1/anti-PD-L1 interaction, that is, anti-PD-1 mAb in anti-PD-L1-R models

and anti-PD-L1 treatment in anti-PD-1-R models. We showed a complete or partial cross-resistance in some models, suggesting that the resistance phenotype was not limited to the antibody used for the selection of resistant models, but to PD-1/PD-L1 checkpoint inhibition axis (Supplementary Fig. S2).

### Therapeutic combinations target infiltrating immune populations that appear with resistance

The immune infiltrate of MC38 WT at basal state comprised mostly of CD11b<sup>+</sup> cells and an equivalent proportion of B cells, T cells, and natural killer (NK) cells, in accordance with other publications (25). Both resistant models showed an increase in CD8<sup>+</sup> T central memory (Tcm) cells, suggesting that ICI therapies were unable to activate these cells properly (Fig. 2A). Conversely, NK-, NKT-, and B-cell contents were decreased in both resistant models in comparison with the WT model (Supplementary Fig. S3A, S3B, S3C, and S3E). In the MC38 anti-PD-1-R model, we observed that tumor-associated macrophages (TAM), particularly M2-like and monocytes-myeloid derived suppressor cells (M-MDSC) were significantly upregulated (Fig. 2B; Supplementary Fig. S3H), whereas in the MC38 anti-PD-L1-R model, total T cells were upregulated, representing up to 20% of CD45<sup>+</sup> cells, as well as the proportion of Tregs (Supplementary Fig. S3G). Examination of the polymorphonuclear-MDSCs (PMN-MDSC) population revealed a trend toward increased infiltration in the MC38 anti-PD-1-R model (Fig. 2C; Supplementary Fig. S3A–S3C). On the basis of the immunophenotypic data and literature data, we evaluated selected therapeutic combinations aiming to target specific immune subsets. On the basis of our data and those reported by Bertrand and colleagues showing that anti-TNF $\alpha$  mAb could enhance anti-PD-1 responses in melanoma, we tested the combination of anti-TNF $\alpha$  with the anti-PD-1 mAb to boost the T-cell response in MC38 anti-PD-1-R model (26). This combination resulted in a significant delay in tumor growth ( $P < 0.05$ ; Fig. 2D). Because this model is one of the most commonly used in immuno-oncology studies, we decided to test other combinations targeting myeloid suppressor cells. We combined anti-CD47 with anti-PD-1 to target the SIRP $\alpha$ -CD47 pathway, a “don’t eat me” phagocytosis checkpoint signal (27). This combination overcame therapeutic resistance to anti-PD-1 in MC38 anti-PD-1-R ( $P < 0.05$ ; Fig. 2E). Moreover, in accordance with the increased infiltration of neutrophils that we detected in the MC38 anti-PD-1-R models, we combined anti-PD-1 with anti-Ly6G, to deplete neutrophils. We observed a significant regression of tumor volume with this combination ( $P < 0.001$ ) in comparison with untreated group (Fig. 2F).

RENCA tumors have previously been reported to contain a dense immune infiltrate, representing up to 60% of total cells at basal state (Supplementary Fig. S4A–S4D; ref. 28). In the RENCA resistant models, we detected the expansion of CD8<sup>+</sup> T cells. The large proportion of CD8<sup>+</sup> Tcm suggests that resistance may be reversed if they are reactivated by targeting other inhibitory checkpoints (Fig. 2G). Indeed, some studies have previously described upregulation of TIM-3 as a mechanism of adaptive resistance to anti-PD-1 therapy (8). Because CD8<sup>+</sup> T cells are abundant in RENCA anti-PD-1-R models, we evaluated therapeutic combinations targeting alternative ICIs. Thus, we performed an *in vivo* survival and antitumor efficacy study with anti-TIM-3, anti-LAG-3 and anti-CTLA-4 mAbs alone or in combination with anti-PD-1 in the anti-PD-1-R RENCA model (Fig. 2H–K). We observed an antitumor effect of the anti-LAG-3 administered as a single agent, whereas anti-TIM-3 and anti-CTLA-4 antibodies used as single agents did not show any efficacy in this resistant model (Fig. 2H). However, in combination with anti-PD-1, these three antibodies induced a significant delay in tumor growth in

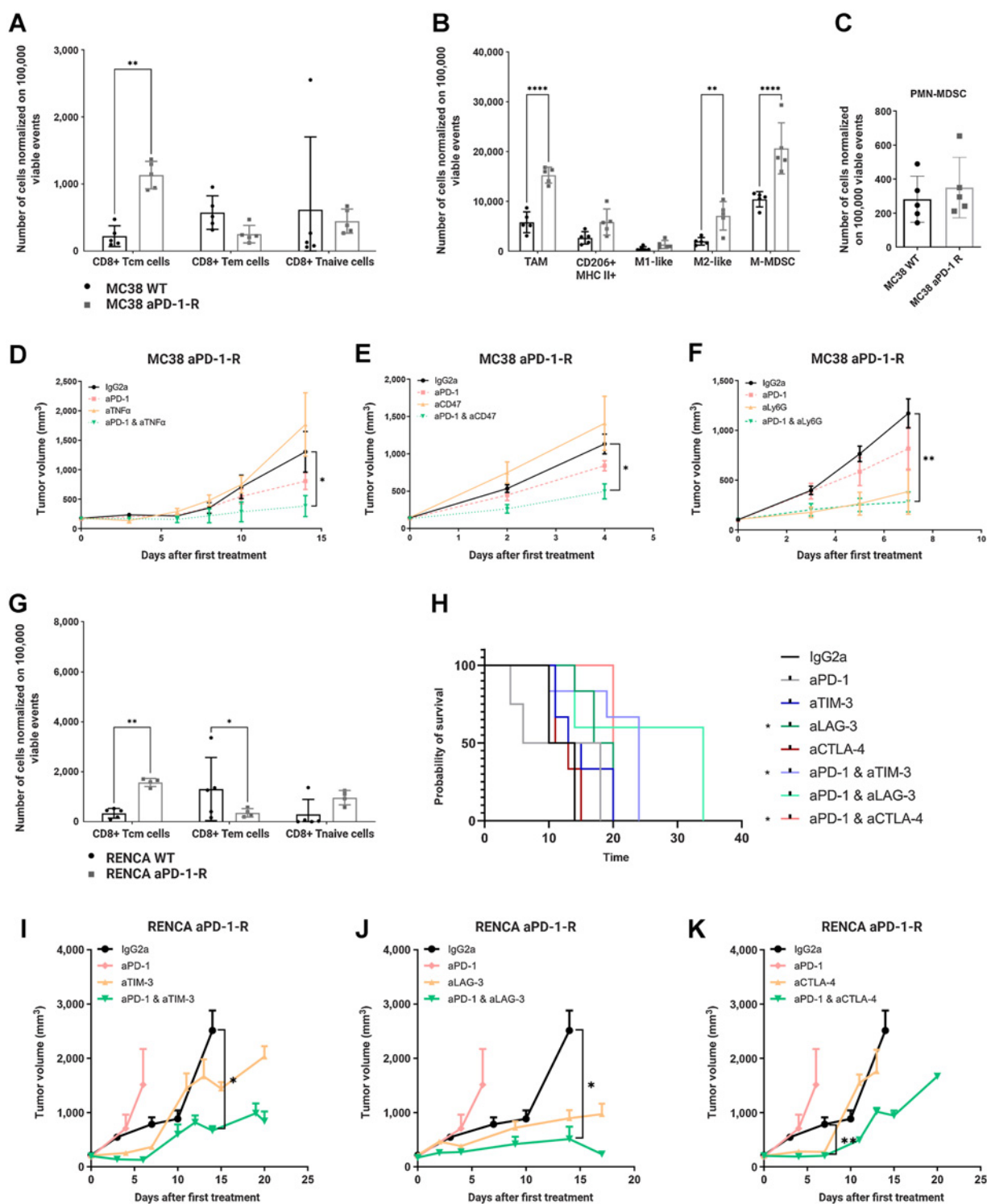


**Figure 2.**

Efficacy of therapeutic combinations *in vivo* in preclinical anti-PD-1-R and anti-PD-L1-R models. **A-C**, Flow cytometry analysis of tumor-infiltrating immune cells in MC38 WT versus MC38 anti-PD-1-R. **D**, C57Bl/6 MC38 anti-PD-1-R model implanted in mice treated with anti-TNF $\alpha$  and anti-PD-1. **E**, C57Bl/6 MC38 anti-PD-1-R model implanted in mice treated with anti-CD47 and anti-PD-1. **F**, C57Bl/6 MC38 anti-PD-1-R model implanted in mice treated with anti-Ly6G and anti-PD-1. **G** and **H**, RENCA WT versus RENCA anti-PD-1-R. **I-K**, BALB/C RENCA anti-PD-1-R model implanted in mice treated with anti-TIM-3 (**I**), anti-LAG-3 (**J**), and anti-CTLA-4 (**K**) and anti-PD-1. Data shown are mean tumor volume values and error bars are  $\pm$  SEM. Significant decreases and increases were assessed by a two-way ANOVA statistical test, with Bonferroni *post hoc* test. For PMN-MDSC cells, significant decreases and increases were assessed by Mann-Whitney *t* test.  $n = 5$  tumors per group, or 3 to 5 mice per group. \*,  $P < 0.05$ ; \*\*,  $P < 0.01$ ; \*\*\*\*,  $P < 0.0001$ .

comparison with the group receiving a combination with an IgG2a control ( $P < 0.05$ ). Moreover, we did not observe adverse toxic effects of these combinations (no effect on body weight or on animal well-being). Overall, these results suggest that resistance to anti-PD-1 or anti-PD-L1 therapy may be circumvented with various combinations targeting other ICIs.

To determine whether Treg depletion could reverse the resistant phenotype we administered anti-CD25 (29) in combination with anti-PD-L1 in the MC38 anti-PD-L1-R model. In this model, the anti-CD25 mAb alone or in combination with anti-PD-L1 induced a trend toward reduced tumor growth ( $P = 0.09$ ; Supplementary Fig. S5A). This modest effect may be due to the fact that activated T cells also express CD25 and may have been depleted by the anti-CD25 mAb. In addition, we investigated whether targeting of MDSC could be of interest. We evaluated anti-CSF1R alone or in combination with anti-PD-1 in MB49 anti-PD-1-R model and we observed a modest trend toward reduced tumor growth with this combination ( $P = 0.1$ ; Supplementary Fig. S5B). In fact, the immune infiltrate of the MB49 WT model comprised of two main populations, represented by PMN-MDSC and CD11b<sup>+</sup> B cells (22% and 35%, respectively; Supplementary Fig. S6A, S6B, S6C, and S6E). In the resistant models, analysis of CD11b<sup>+</sup> cells revealed an increase of the proportion of CD206<sup>+</sup>MHC II<sup>+</sup> macrophages and M-MDSC, which are expected to promote tumor growth (Supplementary Fig. S6H). As opposed to the MC38 variants described above, these data show similar alterations in the immune infiltrates of the two MB49 resistant models, in particular for macrophages and M-MDSC.

#### Identification of genes implicated in the resistance phenotype

We performed gene expression profiling of sensitive and resistant models in an effort to identify pathways and genes of interest with an altered expression in resistant tumors. In gene expression profiling analyses, MC38-resistant models displayed the highest number of alterations in canonical pathways among all the models which we developed (Fig. 3A). Concerning the alterations of gene expression in canonical pathways for MB49 models, only a limited number were found to be upregulated or downregulated, suggesting that these models have not undergone the same degree of genetic modifications. Moreover, profiles were very similar in both anti-PD-1-R and anti-PD-L1-R models. For instance, WNT/ $\beta$ catenin signaling was upregulated in both models, an alteration which was associated with anti-PD-1 resistance correlated with PMN-MDSC accumulation, as observed in our models (Fig. 3A; ref. 30). Similarly to MB49 models, the analysis of canonical pathways suggested that the resistant RENCA variants had not undergone significant genetic modifications (Fig. 3A). Moreover, the results of canonical pathway analyses in MBT-2 were completely different from those in MB49 anti-PD-L1-R models. Many signaling pathways were found to be upregulated, such as HIF1 $\alpha$ , TGF $\beta$ , and ERK/MAPK signaling. These pathways may explain the preferential recruitment of M-MDSC in the immune infiltrate and primary resistance to anti-PD-L1 therapy in this model (Fig. 3A; Supplementary Fig. S7; refs. 31, 32).

Contrary to other resistant models, TyrNras resistant models contained a limited immune infiltrate, assimilating them to “cold tumors” (Supplementary Fig. S8). Unlike the other two models mentioned above, the TyrNras models displayed deregulation of a large number of pathways, suggestive of significant genetic alterations, with different patterns in each model. For instance, in the TyrNras anti-PD-1-R model, pathways that activate T cells (Th1 pathways, cross-talk with dendritic cell (DC) and IFN signaling) were upregulated, whereas these pathways were decreased in the anti-PD-L1-R model. However, the

ILK-signaling pathway, which has been largely associated with tumor progression, was upregulated in both models (33). Moreover, the JAK/STAT signaling pathway was downregulated, in keeping with previous reports implicating JAK1 and 2 in acquired resistance to anti-PD-1 (Fig. 3A; ref. 7).

Finally, using RNA-seq analysis, we identified genes commonly altered in several anti-PD-1-R and anti-PD-L1-R models at basal state. We compared differentially expressed genes within anti-PD-1-resistant models (four models: MC38, MB49, RENCA, and TyrNras) and within anti-PD-L1-resistant models (five models: MC38, MB49, RENCA, TyrNras, and MBT2; Fig. 3B and C, respectively). After analysis, we identified 11 genes commonly altered in at least five of the nine resistant models (Fig. 3D). Among these potential candidate genes, we explored *Serpinf1* and have produced and characterized MC38 variants with reduced or enhanced expression of PEDF and tested the therapeutic sensitivity of an MBT2 variant with reduced expression of PEDF.

#### Altered pigment epithelial-derived factor expression impacts sensitivity to anti-PD-1 and anti-PD-L1

To explore the impact of altered PEDF expression on sensitivity to ICIs, we modulated the expression of this gene by transfecting the MC38 WT cells with an empty vector or one containing full-length *Serpinf1* cDNA. Endogenous *Serpinf1* was also knocked out using CRISPR/Cas9 in the MC38 WT and MBT2 WT models, displaying primary sensitivity and resistance to anti-PD-1 therapy, respectively. To confirm modulation of PEDF protein content, we performed an IHC analysis of PEDF expression in established tumors of MC38 WT and resistant models as well as genetically modified modes (Fig. 4A). PEDF content was found to be strongly increased in the anti-PD-1-R MC38 model, in keeping with the RNA-seq analysis. After having confirmed that tumorigenesis was not impacted by modifications in PEDF expression, we tested these models for sensitivity to anti-PD-1 and anti-PD-L1 therapies. Importantly, the two control cell lines behaved similarly to WT counterparts regarding response to therapies (Fig. 1B and Fig. 4B, C, and G). Induced overexpression of PEDF in MC38 was associated with a loss of sensitivity to anti-PD-1 therapy and reproduced the results observed with our MC38 anti-PD-1-R model obtained by repeated exposure *in vivo* (Fig. 4D). Knockdown of PEDF was associated with enhanced sensitivity to anti-PD-1 therapy in the MC38 model, with observations of complete remissions (Fig. 4E). To understand whether PEDF might be associated with a primary resistance phenotype also, we evaluated the impact of PEDF downregulation in the MBT2 model (Fig. 4F). We obtained a partial response to anti-PD-1 when PEDF content was reduced (Fig. 4H). Together, these results suggest that overexpression of PEDF induced resistance to anti-PD-1 therapy.

#### Anti-PD-1 resistance and pigment epithelial-derived factor overexpression induced preferential accumulation of saturated fatty acids and monounsaturated fatty acids

To better understand the involvement of *Serpinf1* in the process of anti-PD-1 resistance and explore the hypothesis supported by RNA-seq analysis, we studied lipid accumulation in our models. We performed staining with ORO to evaluate accumulation of neutral lipids and lipid droplets. As PEDF may bind to ATGL and catalyze the hydrolysis reaction of triacylglycerols to diacylglycerols, we also analyzed ATGL expression by IHC. Comparison of the WT parental and the anti-PD-1-R models showed that lipid droplets were not detected in the sensitive model, whereas several zones of tumor cells gorged with lipid droplets were present in the resistant model.

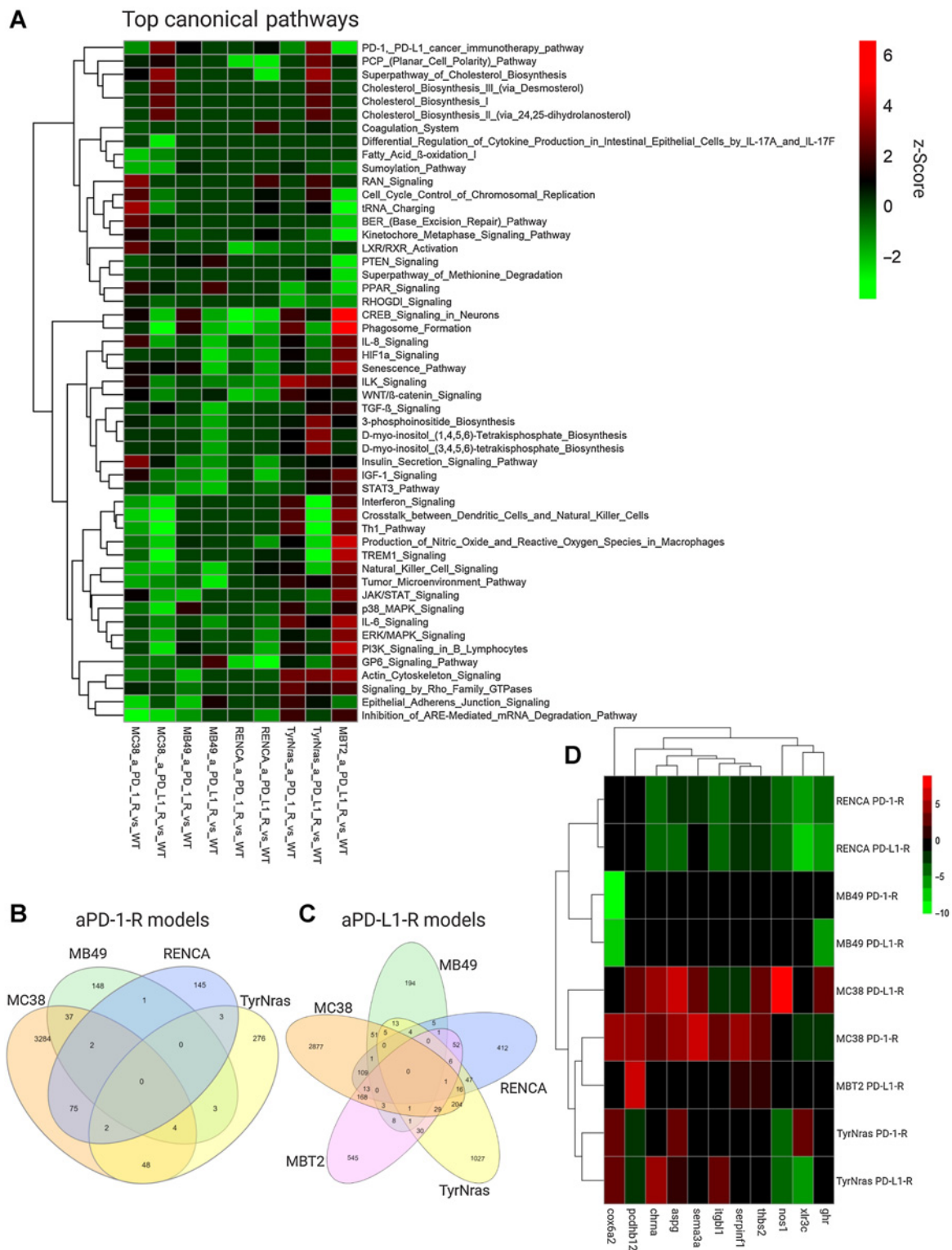


**Figure 3.** Identification of altered genes in anti-PD-1-R and anti-PD-L1-R models by RNA-seq analysis. **A**, Heat map of RNA-seq expression z-scores displaying the prediction of deregulated pathways due to the acquisition of anti-PD-1 or anti-PD-L1 resistance. The top five upregulated and downregulated pathways for each model were selected and grouped. **B**, Venn diagram representation of gene modulation shared with anti-PD-1-resistant colorectal cancer (MC38), renal cell carcinoma (RENCA) and bladder cancer (MB49) and melanoma cancer (TyrNras). **C**, Venn diagram representation of gene modulation shared with anti-PD-L1-resistant colorectal cancer (MC38), renal cell carcinoma (RENCA), bladder cancer (MB49) and bladder cancer (MBT-2) and melanoma cancer (TyrNras), with a consideration of  $P < 0.05$  and a fold change  $\pm 1$ . **D**, Heat map representing genes commonly modulated in at least five resistant models.

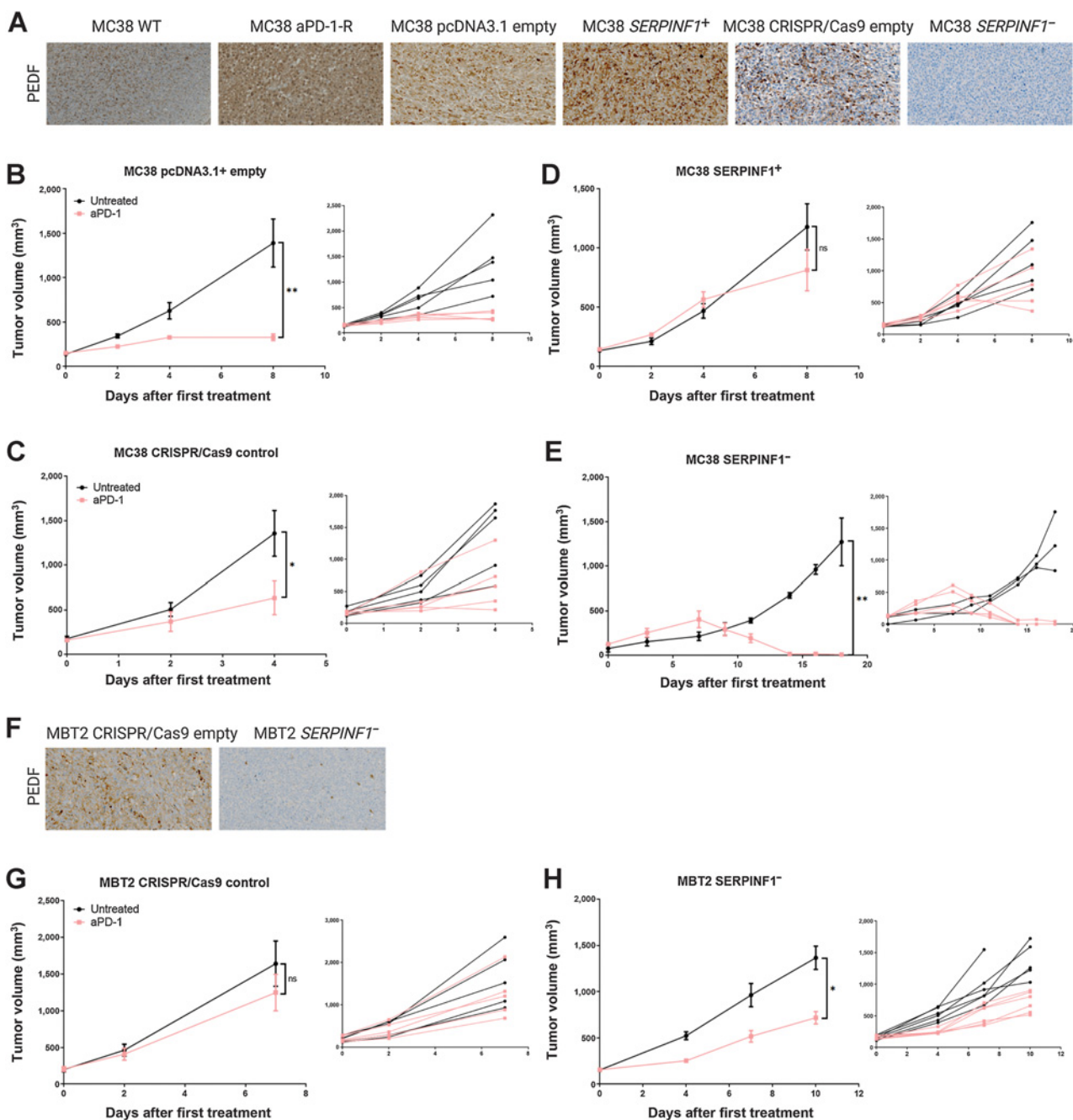


**Figure 4.**

Altered sensitivity profiles to anti-PD-1 associated with modulation of the expression of *Serpinf1* gene. **A**, IHC analysis for PEDF in representative MC38 WT, MC38 anti-PD-1-R, MC38 *Serpinf1*<sup>+</sup>, MC38 *Serpinf1*<sup>-</sup> and control tumors. **B-E**, Tumor growth of MC38 pcDNA3.1+ empty (**B**), MC38 CRISPR/Cas9 control (**C**), MC38 *Serpinf1*<sup>+</sup> (**D**), and MC38 *Serpinf1*<sup>-</sup> (**E**). **F**, IHC analysis for PEDF in representative MBT2 *Serpinf1*<sup>-</sup> and control tumor. MBT2 CRISPR/Cas9 control (**G** and **H**), MBT2 *Serpinf1*<sup>-</sup> (**H**). Data shown are mean tumor volume values and error bars are  $\pm$  SEM.  $n = 3$  or 5 mice per group; \*,  $P < 0.05$ ; \*\*,  $P < 0.01$ , using Mann-Whitney  $t$  test.

Similarly, ATGL staining was found to be more intense in the resistant models than in the sensitive models (**Fig. 5A**).

We then performed gas chromatography detection of fatty acids present in our various tumors. This assay revealed a preferential increase in saturated fatty acids (SFA) and monounsaturated fatty acids (MUFA) in the anti-PD-1 resistant models (MC38 anti-PD-1-R

and MC38 *Serpinf1*<sup>+</sup>) compared with the corresponding sensitive models (MC38 WT and MC38 pcDNA3.1 + empty). In the MC38 *Serpinf1*<sup>-</sup> model, an inversion of these fatty acids, namely polyunsaturated fatty acids (PUFA) to the detriment of SFAs and MUFAs, was detected. All these data confirmed an effect of *Serpinf1* in the fatty acid composition in the tumor (**Fig. 5B-D**).

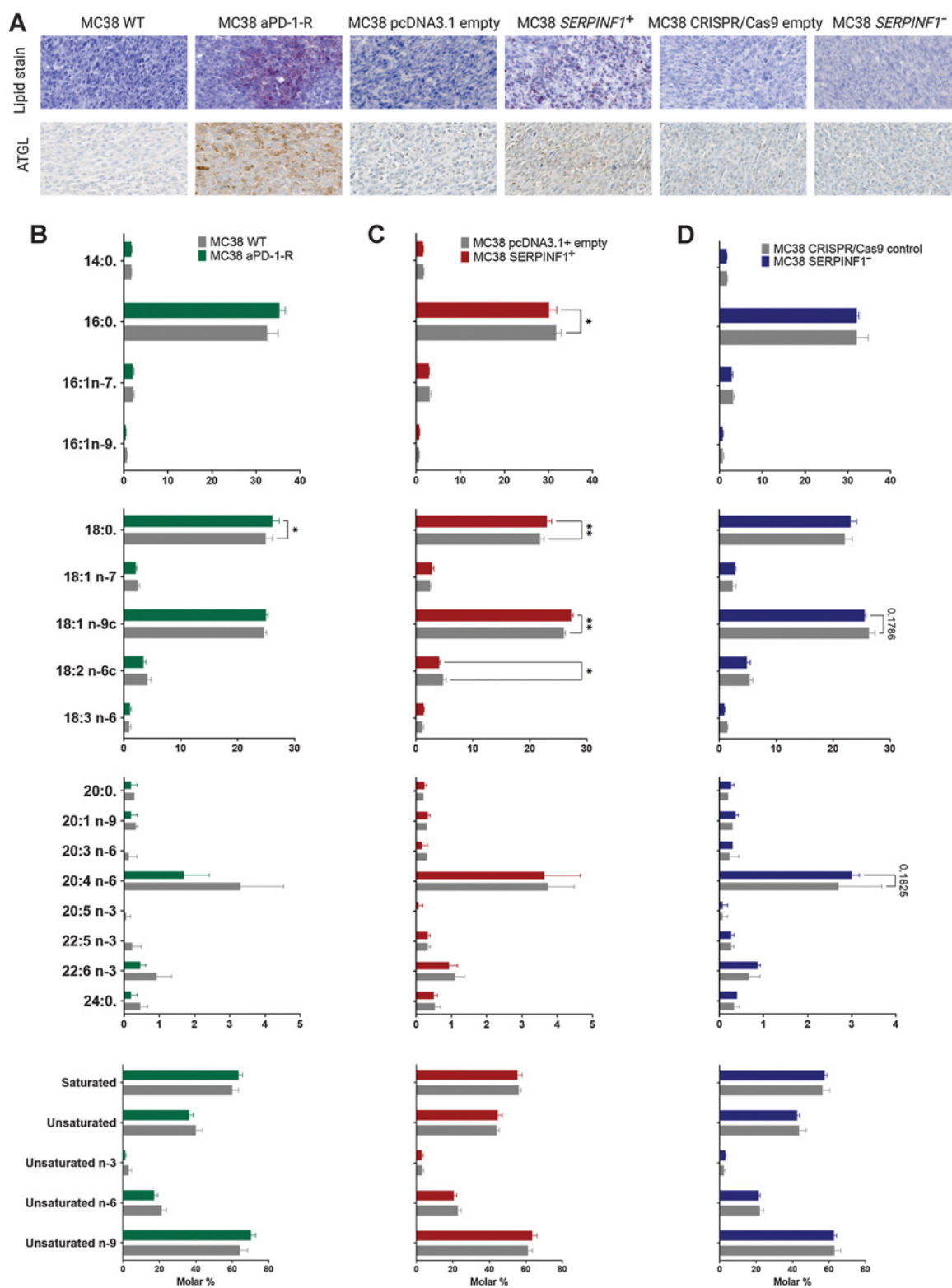


**Figure 5.** SFA and MUFA preferentially accumulate in anti-PD-1-resistant tumors. **A**, Representative pictures of ORO and ATGL staining in all MC38 models. **B–D**, Histograms represent fatty acid composition in tumors in molar percentage (nmol/g). MC38 WT and MC38 anti-PD-1-R models (**B**), MC38 pcDNA3.1 empty and *Serpinf1*<sup>+</sup> (**C**), MC38 CRISPR/Cas9 control and *Serpinf1*<sup>-</sup> (**D**). Significant decreases and increases were assessed by a two-way ANOVA statistical test, with Bonferroni *post hoc* test, \*,  $P < 0.05$ ; \*\*,  $P < 0.01$ ; and \*\*\*\*,  $P < 0.0001$ ,  $n = 3$  tumors per group.

### Impact of tumor pigment epithelial-derived factor expression on microenvironmental T cells

To establish whether increased PEDF expression in resistant tumors could have an impact on T cells present in the tumor immune microenvironment, we performed three complementary experiments. The first was the costaining of ORO with CD8 labeling by IHC. We observed that CD8<sup>+</sup> T cells had a sparse distribution in the MC38 WT model, whereas CD8<sup>+</sup> T cells preferentially accumulated in the islands of tumor cells gorged with lipid droplets in the MC38 anti-PD-1-R model (Fig. 6A). In the second approach, we analyzed the immune infiltrate after exposure of tumors to anti-PD-1 and performed flow cytometry to demonstrate whether the CD8<sup>+</sup> T-cell status was altered in the resistant models (MC38 anti-PD-1-R and MC38 *Serpinf1*<sup>+</sup>). The immune infiltrates of the tumor microenvironment were characterized 24 hours after a second weekly treatment of the selected antibody. First, we observed Th1 CD4<sup>+</sup> T-cell activation using the T-Bet marker. In the two sensitive models, namely MC38 WT and MC38 *Serpinf1*<sup>-</sup>, this subpopulation increased, whereas resistant models followed a downward trend (Fig. 6B). Moreover, the proportion and the activity (granzyme B<sup>+</sup>) of infiltrated CD8<sup>+</sup> T cells decreased in the MC38 *Serpinf1*<sup>+</sup> and MC38 anti-PD-1-R models, whereas it was increased in the MC38 *Serpinf1*<sup>-</sup> and MC38 WT models (Fig. 6C and D). These results indicate that overexpression of *Serpinf1* promotes an immunosuppressive microenvironment. Moreover, these results suggest that *Serpinf1* may be deleterious for the maintenance of antitumor immunity supported by CD8<sup>+</sup> T-cell and Th1 CD4<sup>+</sup> T-cell responses.

Finally, to determine whether the resistant phenotype was supported by the accumulation of FA, we combined anti-PD-1 with orlistat, an inhibitor of fatty acid synthesis that targets ATGL, in the MC38 WT and anti-PD-1-R models. This combination overcame therapeutic resistance to anti-PD-1 in MC38 anti-PD-1-R ( $P < 0.01$ ) and improved survival compared with the untreated group, whereas no effect was detected in MC38 WT model (Fig. 6E and F).

## Discussion

Developing models of acquired resistance to anti-PD-1 or anti-PD-L1 therapies is challenging, as *in vitro* models poorly reproduce their antitumor potential. An important advantage of our *in vivo* resistant models is that the derived variants may be compared with their sensitive parental counterparts, providing insights into potential resistance mechanisms. This is not achievable with *de novo* resistant models to anti-PD-1 and anti-PD-L1 therapies, which, to our knowledge, represent the majority of murine syngeneic models. The availability of several resistant variants additionally allows for identification of common alterations, which are more likely to be mechanistically involved in resistance and can secondarily be validated by modifications of the parental models. Conversely, limitations of this approach include the fact that the tumors used were implanted subcutaneously rather than orthotopically, a factor that may affect the infiltration by the immune system and thus the development of resistance and the relevance to clinical settings. Another caveat of our design is the use of rat anti-murine PD-1/PD-L1 antibodies, given the unavailability of commercially available murine antibodies against these targets. However, this strategy has allowed us to produce variants from several tumor types that may be of great use to characterize the immunologic diversity of tumors, and thus better reproduce the situations encountered in humans.

To understand the role of tumor immune microenvironment alterations in acquired resistance to anti-PD-1/L1 targeted therapies,

we first analyzed the tumor immune microenvironment in syngeneic WT and anti-PD-1 and/or anti-PD-L1 resistant models. A possible mechanism of acquired resistance to anti-PD-1/L1 therapies is the insufficient activation of cytotoxic T cells. Focusing on MC38-resistant models, we observed that immune infiltrates at basal state were different in the two resistant models. As MC38 anti-PD-1-R model displayed an upregulation of CD8<sup>+</sup> Tcm cells, we tested the combination of anti-PD-1 with anti-TNF $\alpha$ . In accordance with the report by Bertrand and colleagues that TNF $\alpha$  or TNFR blockade could enhance the activity of anti-PD-1-directed therapy in melanomas, we found that the combination of anti-TNF $\alpha$  with anti-PD-1 was able to circumvent resistance in the anti-PD-1-R MC38 tumor model (26). These results support the hypothesis that TNF-targeted agents used in combination with ICIs have the potential to revert some cases of resistance to anti-PD-1/PD-L1-targeted therapies (34). Another hypothesis may be that resistant tumors are enriched in Tregs which hamper the antitumor response. Our results showed a significant increase in the content of FoxP3<sup>+</sup>CD4<sup>+</sup> cells in anti-PD-L1-R MC38 and MB49 models compared with their parental sensitive models, suggesting a role of regulatory T cells in the resistance phenotype. To determine whether Treg depletion could reverse the phenotype, we administered anti-CD25 (29), concomitantly or prior to anti-PD-L1 therapy in our MC38 anti-PD-L1-R model and observed a modest trend toward sensitization for the combination ( $P < 0.1$ ). The absence of a significant combinatorial effect may, however, be explained by the fact that anti-CD25 is likely to deplete not only preexisting Tregs, but also anti-PD-L1-induced activated cytotoxic T cells. Moreover, the use of the PC-61 anti-CD25 is controversial, because results obtained with this antibody have shown a failure to deplete intratumoral Tregs (35).

The role of myeloid suppressor cells in the resistance to ICIs remains poorly understood. Several approaches may be considered to circumvent resistance, including therapeutic modulation of myeloid checkpoints or depletion of protumor populations. CD47 expressed by tumor cells is a promising target, since its interaction with SIRP $\alpha$  present on macrophages has been shown to inhibit tumor cell phagocytosis (36). In addition, CD47/SIRP $\alpha$  may impact the activation of cytotoxic CD8<sup>+</sup> T cells through DC antigen presentation (37). Using our MC38 anti-PD-1-R model, we found that combination of anti-PD-1 with anti-CD47 indeed overcame the PD-1 resistance. In this same model, we observed a significant increase in the intratumor neutrophil content, which is remarkable because the MC38 model is known to lack neutrophils in the tumor microenvironment (25). Depletion of neutrophils using anti-Ly6G in combination with anti-PD-1 was found to overcome resistance in the MC38 anti-PD-1-R model. In other cases, myeloid cells are largely represented before therapy and may yet increase in response to therapy (38). To model this situation, we used the MB49 WT tumor in which we observed an increase of TAM and M-MDSC in the resistant models and administered anti-CSF1R in the MB49 anti-PD-1-R model to target type 2 macrophages in an attempt to restore the activity of anti-PD-1. With this combination, we observed a nonsignificant trend suggesting enhanced activity of the combination on tumor growth, in spite of the depletion of macrophages, possibly due to a compensatory increase of Treg cells (39).

Data from the literature support the hypothesis that upregulation of alternative immune checkpoints is associated with resistance to anti-PD-1 therapy. Thommen and colleagues established a correlation between the expression of multiple immune checkpoints on CD8<sup>+</sup> T cells and disease progression in patients with NSCLC (40). Koyama and colleagues observed IC overexpression, notably of TIM-3, in T

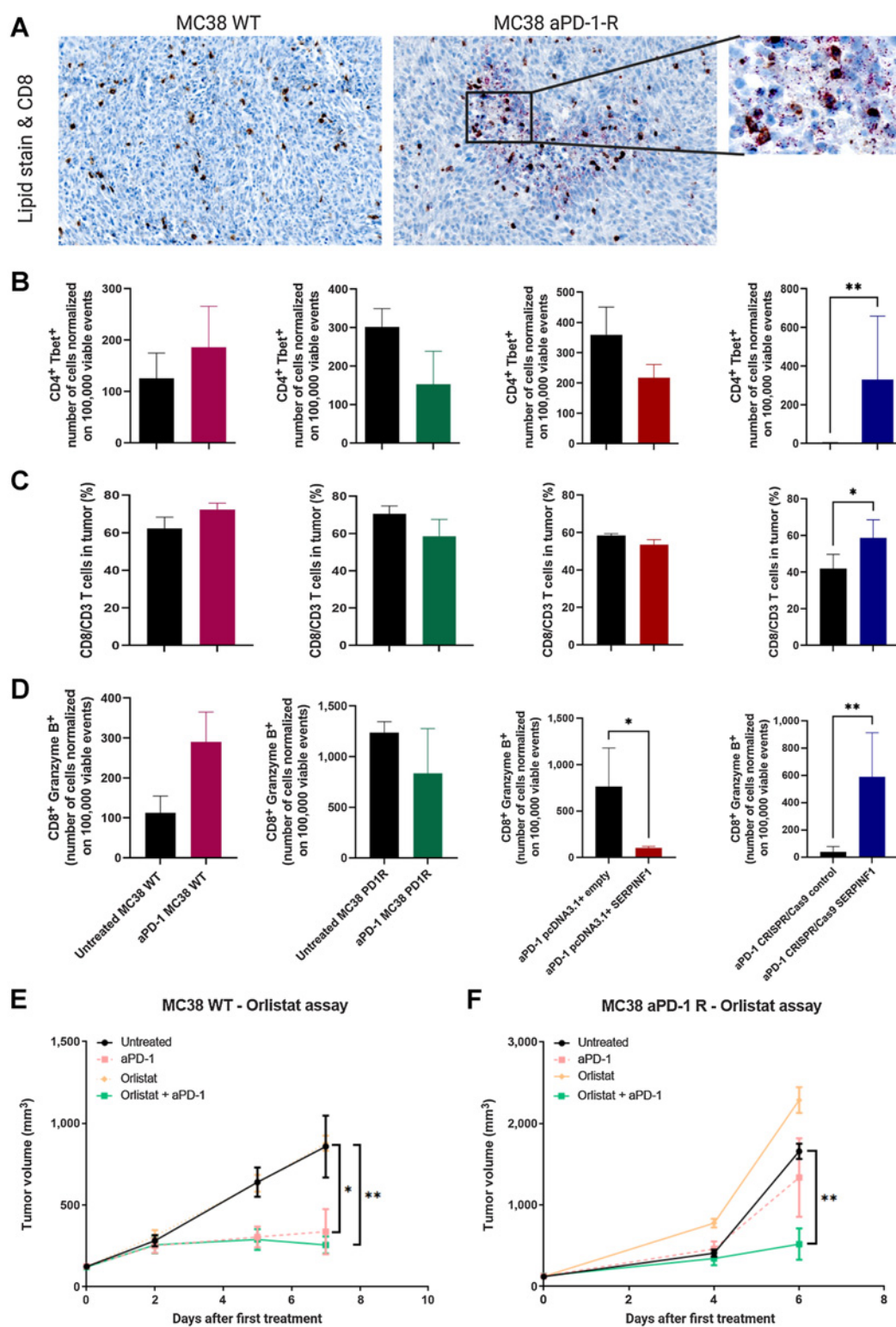


**Figure 6.**

*Serpinf1* inhibition enhances cytotoxic lymphocyte responses. **A**, Representative pictures of ORO lipid staining and CD8<sup>+</sup> staining. **B–D**, Flow cytometry analysis of tumor-infiltrating immune cell populations in tumor models treated with anti-PD-1. CD4<sup>+</sup> Tbet<sup>+</sup> T cells (**B**), percentage of CD3<sup>+</sup>/CD8<sup>+</sup> ratio (**C**), and CD8<sup>+</sup> granzyme B<sup>+</sup> T cells (**D**). **E** and **F**, Tumor models treated with anti-PD-1, Orlistat or a combination of both agents MC38 WT (**E**), MC38 anti-PD-1-R (**F**). Data shown are mean tumor volume values and error bars are  $\pm$  SEM.  $n = 4-5$  tumors per group or 5 or 6 mice per group. Significant decreases and increases were assessed by a Mann-Whitney  $t$  test, \*,  $P < 0.05$  and \*\*,  $P < 0.01$ .

cells associated with adaptive resistance to anti-PD-1 (8). TIM-3 expression by tumor cells has been linked to a poor prognosis in liver cancer, melanoma, lung cancer, and renal cancer (41). Moreover, tumor cell lines expressing TIM-3 had stronger self-renewal capacities compared with cells with no TIM-3 expression (42). Although the TIM-3 ligand recognized by tumor cells remains unknown, studies have shown that TIM-3 engagement can activate the NF $\kappa$ B pathway (43), thereby contributing to acquired resistance through the acquisition of cancer stemness properties (44). To determine the role of alternative IC targeting in our resistant models, we evaluated anti-TIM-3, anti-CTLA-4, and anti-LAG-3 mAbs alone or in combination with anti-PD-1 in RENCA anti-PD-1-R cells, because of the large amount of CD8<sup>+</sup> T cells present in this model. We observed a significant antitumor effect of all of these combinations in this resistant model, with a good tolerance of the combination regimens. Overall, these data support the combination of ICI-targeted therapies as a strategy in patients with resistant disease.

Knowledge regarding tumor cell molecular alterations associated with anti-PD-1 acquired resistance remains limited, with a major focus on the role of tumor mutation burden (TMB) and neoantigenic depletion (45). Zaretsky and colleagues described mutations in *Jak1* and *Jak2* genes in resistant melanoma tumors (7), whereas Garcia-Diaz and colleagues reported that an IFN signature enrichment enhanced PD-L1 and PD-L2 expression in melanoma cells (46). To identify molecular alterations mechanistically involved in resistance to anti-PD-1 and/or anti-PD-L1 targeted therapy, we performed an RNA-seq analysis, comparing sensitive parental models and their resistant counterparts. We then determined common modifications of genes between anti-PD-1-R and anti-PD-L1-R tumors. This approach may be used to identify putative pathways and candidate genes involved in the *in vivo* resistance phenotype. In the MC38, MBT2, and TyrNras models, we observed alterations of the pathways already described as being modified in patients with disease progressing under ICI therapy, such as PTEN, IFN $\gamma$ , PI3K/AKT or JAK1/JAK2. However, this appears to be highly model dependent, reflecting the heterogeneity observed in patients. Models such as MB49 and RENCA display relatively few modifications of their expression profile upon acquisition of a resistant phenotype, which suggests an environment with a low TMB and therefore possibly less immunogenic. Insofar as the degree of immune infiltration is not directly correlated to tumor immunogenicity, this observation could partially explain why RENCA models grow in spite of a significant immune infiltration.

Our results support a potential role of the *Serpinf1* gene in resistance to anti-PD-1 therapy. *Serpinf1* codes for PEDF, which has mainly been studied as a secreted protein, is reported to inhibit cancer cell proliferation, and increase apoptosis via the FAS/FASL pathway, and reduce VEGF expression by cancer cells (47). However, intracellular PEDF has also been shown to regulate several pathways, including fatty acid metabolism. To our knowledge, the impact of PEDF on sensitivity to ICI therapy has not yet been explored. PEDF was found to be overexpressed both at the transcriptional and protein level in MC38 anti-PD-1-R model. To validate *Serpinf1* as a candidate gene involved in resistance to therapy in the MC38 model, we developed variants with upregulation or downregulation of PEDF. We found that the MC38 variant that overexpressed PEDF was resistant to anti-PD-1 targeted therapy. In addition, the *Serpinf1* knockout model appeared to be highly sensitive to anti-PD-1, with complete remission in some of mice, whereas the models transfected with the control vectors displayed partial response at best. These results suggest that PEDF may be mechanistically involved in the acquisition of a resistance phenotype to ICIs, in particular to anti-PD-1-based therapy.

Overexpression of PEDF has been reported to be associated with altered AMPK activity, particularly in obesity-associated insulin resistance (48). RNA-seq analysis of our resistant MC38 model was compatible with enhanced resistance to insulin, whereas the FAO pathway was underexpressed. We hypothesized that PEDF overexpression in resistant cancer cells is associated with enhanced *de novo* lipogenesis (15) and an increase of SFA and MUFA fatty acids in the anti-PD-1-resistant models. These results are in agreement with a study which showed the beneficial antitumor effect of PUFAs in contrast to SFAs and MUFAs (49). This allows cells enhanced flexibility to distribute FFAs in different biosynthetic pathways and generate a diverse pool of lipid species with distinct functions. Beyond contribution to the energy pool, which is undeniably advantageous for cancer cells, if SFA and MUFA are produced, FFA can be released, inducing an inflammatory microenvironment. This in turn might increase the pool of protumor cells, such as MDSCs and TAM, while also blocking CD8<sup>+</sup> T-cell activation (50), a hypothesis which was supported by the colocalization of lipid droplets and CD8<sup>+</sup> staining in our resistant model. Moreover, flow cytometry experiment confirmed that the proportion and activation of CD8<sup>+</sup> T cells were correlated with the expression of PEDF.

It has been reported that the binding of PD-L1 to PD-1 causes the metabolic reprogramming of cytotoxic CD8<sup>+</sup> cells from aerobic glycolysis to free FAO, thereby inducing a phenotypic conversion of effector T cells into exhausted cells (16, 18). Because PD-1 binding has been shown to activate FAO, we hypothesize that increased FFA production and release induced by increased PEDF within tumor cells might lead the polarization of CD8<sup>+</sup> T cells and prevent their activation (16, 17). Consistent with our hypothesis, we obtained durable tumor responses when we combined an anti-fatty acid agent with anti-PD-1 in the MC38 anti-PD-1-R model.

## Conclusion

Resistance to anti-PD-1 and anti-PD-L1 therapy is associated with several genetic alterations and/or modifications in the immune cell infiltrate. Our model library, which may be enriched in the future with several other variants developed using the same methodology, provides an innovative tool to better apprehend the complexity, multifactorial nature and diversity of resistance to ICIs and test resistance reversal strategies.

## Authors' Disclosures

M. Denis reports grants from ANRT and other support from Antineo during the conduct of the study. E. Kress reports grants from ANRT (French government) and other support from DGFIP (French government) during the conduct of the study; other support from Bioetchs outside the submitted work; and Models described in this publication are proposed on a fee for service basis by Antineo. C. Klein reports other support from Roche during the conduct of the study; other support from Roche outside the submitted work. C. Dumontet reports grants from Roche outside the submitted work; and Models contained in this article may be analyzed on a fee-for-service basis by Antineo. No disclosures were reported by the other authors.

## Authors' Contributions

**M. Denis:** Conceptualization, data curation, formal analysis, validation, investigation, visualization, writing—original draft. **C. Grasselly:** Conceptualization, formal analysis, supervision, writing—review and editing. **P.-A. Choffour:** Conceptualization, formal analysis, supervision. **A. Wierinckx:** Software, formal analysis, investigation, visualization. **D. Mathé:** Conceptualization, formal analysis, supervision. **K. Chettab:** Conceptualization, software, formal analysis. **A. Tourette:** Investigation. **N. Talhi:** Investigation. **A. Bourguignon:** Funding acquisition. **F. Birzele:** Software, formal analysis. **E. Kress:** Writing—review and editing. **L.P. Jordheim:** Writing—review

and editing. **C. Klein:** Funding acquisition, writing–review and editing. **E.-L. Matera:** Conceptualization, formal analysis, writing–review and editing. **C. Dumontet:** Supervision, writing–review and editing.

### Acknowledgments

We would also thank all the platform of the SFR Lyon-East platforms (CYCLE). More precisely, the CIQLE platform of University Claude Bernard Lyon 1. The flow cytometry platform of the CRCL U1052/CLB/SFR, the SCAR platform, and ProfileXpert platform, Lyon, France. We acknowledge also Roche, Penzberg Germany platform, and the functional lipidomics platform, INSA Lyon, CNRS, LAMCOS, UMR5259, 69621 Villeurbanne, France. This work was supported in part by the Lyric

Grant (INCa-DGOS-4664). This work was supported by the SIRIC LYriCAN (INCa-DGOS-Inserm\_12563). The National Association Research and Technology (ANRT) supported C. Grasselly and M. Denis for their PhD thesis (CIFRE funding). Figures were created with BioRender.com.

The costs of publication of this article were defrayed in part by the payment of page charges. This article must therefore be hereby marked *advertisement* in accordance with 18 U.S.C. Section 1734 solely to indicate this fact.

Received September 22, 2021; revised January 28, 2022; accepted June 3, 2022; published first June 8, 2022.

### References

- Balar AV, Galsky MD, Rosenberg JE, Powles T, Petrylak DP, Bellmunt J, et al. Atezolizumab as first-line treatment in cisplatin-ineligible patients with locally advanced and metastatic urothelial carcinoma: a single-arm, multicentre, phase 2 trial. *Lancet North Am Ed* 2017;389:67–76.
- Cella D, Grünwald V, Escudier B, Hammers HJ, George S, Nathan P, et al. Patient-reported outcomes of patients with advanced renal cell carcinoma treated with nivolumab plus ipilimumab versus sunitinib (CheckMate 214): a randomised, phase 3 trial. *Lancet Oncol* 2019;20:297–310.
- Garon EB, Rizvi NA, Hui R, Leighl N, Balmanoukian AS, Eder JP, et al. Pembrolizumab for the treatment of non–small-cell lung cancer. *N Engl J Med* 2015;372:2018–28.
- Larkin J, Chiarion-Sileni V, Gonzalez R, Grob J-J, Rutkowski P, Lao CD, et al. Five-year survival with combined nivolumab and ipilimumab in advanced melanoma. *N Engl J Med* 2019;381:1535–46.
- Alsaab HO, Sau S, Alzhrani R, Tatiparti K, Bhise K, Kashaw SK, et al. PD-1 and PD-L1 checkpoint signaling inhibition for cancer immunotherapy: mechanism, combinations, and clinical outcome. *Front Pharmacol* 2017;8:561.
- Spranger S, Bao R, Gajewski TF. Melanoma-intrinsic  $\beta$ -catenin signalling prevents anti-tumour immunity. *Nature* 2015;523:231–5.
- Zaretsky JM, Garcia-Diaz A, Shin DS, Escuin-Ordinas H, Hugo W, Hu-Lieskovan S, et al. Mutations associated with acquired resistance to PD-1 blockade in melanoma. *N Engl J Med* 2016;375:819–29.
- Koyama S, Akbay EA, Li YY, Herter-Sprie GS, Buczkowski KA, Richards WG, et al. Adaptive resistance to therapeutic PD-1 blockade is associated with upregulation of alternative immune checkpoints. *Nat Commun* 2016;7:10501.
- Schoenfeld AJ, Hellmann MD. Acquired resistance to immune checkpoint inhibitors. *Cancer Cell* 2020;37:443–55.
- Steele FR, Chader GJ, Johnson LV, Tombran-Tink J. Pigment epithelium-derived factor: neurotrophic activity and identification as a member of the serine protease inhibitor gene family. *Proc Natl Acad Sci U S A* 1993;90:1526–30.
- Famulla S, Lamers D, Hartwig S, Passlack W, Horrihgs A, Cramer A, et al. Pigment epithelium-derived factor (PEDF) is one of the most abundant proteins secreted by human adipocytes and induces insulin resistance and inflammatory signaling in muscle and fat cells. *Int J Obes* 2011;35:762–72.
- Abe R, Shimizu T, Yamagishi S-I, Shibaki A, Amano S, Inagaki Y, et al. Over-expression of pigment epithelium-derived factor decreases angiogenesis and inhibits the growth of human malignant melanoma cells *in vivo*. *Am J Pathol* 2004;164:1225–32.
- Chen Z, Che D, Gu X, Lin J, Deng J, Jiang P, et al. Upregulation of PEDF predicts a poor prognosis and promotes esophageal squamous cell carcinoma progression by modulating the MAPK/ERK signaling pathway. *Front Oncol* 2021;11:625612.
- Singh RB, Blanco T, Mittal SK, Alemi H, Chauhan SK, Chen Y, et al. Pigment epithelium-derived factor enhances the suppressive phenotype of regulatory T cells in a murine model of dry eye disease. *Am J Pathol* 2021;191:720–9.
- Li C, Huang Z, Zhu L, Yu X, Gao T, Feng J, et al. The contrary intracellular and extracellular functions of PEDF in HCC development. *Cell Death Dis* 2019;10:742.
- Patsoukis N, Bardhan K, Chatterjee P, Sari D, Liu B, Bell LN, et al. PD-1 alters T-cell metabolic reprogramming by inhibiting glycolysis and promoting lipolysis and fatty acid oxidation. *Nat Commun* 2015;6:6692.
- O’Sullivan D, van der Windt GJW, Huang SC-C, Curtis JD, Chang C-H, Buck MD, et al. Memory CD8+ T cells use cell-intrinsic lipolysis to support the metabolic programming necessary for development. *Immunity* 2018;49:375–6.
- Pearce EL, Walsh MC, Cejas PJ, Harms GM, Shen H, Wang L-S, et al. Enhancing CD8 T-cell memory by modulating fatty acid metabolism. *Nature* 2009;460:103–7.
- Percie du Sert N, Ahluwalia A, Alam S, Avey MT, Baker M, Browne WJ, et al. Reporting animal research: explanation and elaboration for the ARRIVE guidelines 2.0. *PLoS Biol* 2020;18:e3000411.
- Trapnell C, Williams BA, Pertea G, Mortazavi A, Kwan G, van Baren MJ, et al. Transcript assembly and quantification by RNA-Seq reveals unannotated transcripts and isoform switching during cell differentiation. *Nat Biotechnol* 2010;28:511–5.
- Wu TD, Reeder J, Lawrence M, Becker G, Brauer MJ. GMAP and GSNAP for genomic sequence alignment: enhancements to speed, accuracy, and functionality. In: Mathé E, Davis S, editors. *Statistical genomics. Methods in Molecular Biology*, vol 1418. New York: Humana Press; 2016.
- Mortazavi A, Williams BA, McCue K, Schaeffer L, Wold B. Mapping and quantifying mammalian transcriptomes by RNA-seq. *Nat Methods* 2008;5:621–8.
- Ritchie ME, Phipson B, Wu D, Hu Y, Law CW, Shi W, et al. limma powers differential expression analyses for RNA-sequencing and microarray studies. *Nucleic Acids Res* 2015;43:e47.
- Heberle H, Meirelles GV, da Silva FR, Telles GP, Minghim R. InteractiVenn: a web-based tool for the analysis of sets through Venn diagrams. *BMC Bioinformatics* 2015;16:169.
- Taylor MA, Hughes AM, Walton J, Coenen-Stass AML, Magiera L, Mooney L, et al. Longitudinal immune characterization of syngeneic tumor models to enable model selection for immune oncology drug discovery. *J Immunother Cancer* 2019;7:328.
- Bertrand F, Montfort A, Marcheteau E, Imbert C, Gilhodes J, Filleron T, et al. TNF $\alpha$  blockade overcomes resistance to anti-PD-1 in experimental melanoma. *Nat Commun* 2017;8:2256.
- Feng M, Jiang W, Kim BY, Zhang C, Fu Y-X, Weissman IL. Phagocytosis checkpoints as new targets for cancer immunotherapy. *Nat Rev Cancer* 2019;19:568–86.
- Jw Yu, Bhattacharya S, Yanamandra N, Kilian D, Shi H, Yadavilli S, et al. Tumor-immune profiling of murine syngeneic tumor models as a framework to guide mechanistic studies and predict therapy response in distinct tumor microenvironments. *PLoS One* 2018;13:e0206223.
- Setiady YY, Coccia JA, Park PU. *In vivo* depletion of CD4+FOXP3+ Treg cells by the PC61 anti-CD25 monoclonal antibody is mediated by Fc $\gamma$ IIIb+ phagocytes. *Eur J Immunol* 2010;40:780–6.
- DeVito NC, Sturdivant M, Thievanthiran B, Xiao C, Plebanek MP, Salama AKS, et al. Pharmacological Wnt ligand inhibition overcomes key tumor-mediated resistance pathways to anti-PD-1 immunotherapy. *Cell Rep* 2021;35:109071.
- Yang Z, Guo J, Weng L, Tang W, Jin S, Ma W. Myeloid-derived suppressor cells—new and exciting players in lung cancer. *J Hematol Oncol* 2020;13:10.
- Chiu DK-C, Tse AP-W, Xu IM-J, Di Cui J, Lai RK-H, Li LL, et al. Hypoxia inducible factor HIF-1 promotes myeloid-derived suppressor cells accumulation through ENTPD2/CD39L1 in hepatocellular carcinoma. *Nat Commun* 2017;8:517.
- Zheng C-C, Hu H-F, Hong P, Zhang Q-H, Xu WW, He Q-Y, et al. Significance of integrin-linked kinase (ILK) in tumorigenesis and its potential implication as a biomarker and therapeutic target for human cancer. *Am J Cancer Res* 2019;9:186–97.
- Fischer R, Kontermann RE, Pfizenmaier K. Selective targeting of TNF receptors as a novel therapeutic approach. *Front Cell Dev Biol* 2020;8:401.

35. Arce Vargas F, Furness AJS, Solomon I, Joshi K, Mekkaoui L, Lesko MH, et al. Fc-optimized anti-CD25 depletes tumor-infiltrating regulatory T cells and synergizes with PD-1 blockade to eradicate established tumors. *Immunity* 2017;46:577–86.
36. Willingham SB, Volkmer J-P, Gentles AJ, Sahoo D, Dalerba P, Mitra SS, et al. The CD47-signal regulatory protein alpha (SIRPa) interaction is a therapeutic target for human solid tumors. *Proc Natl Acad Sci U S A* 2012;109:6662–7.
37. Liu X, Pu Y, Cron K, Deng L, Kline J, Frazier WA, et al. CD47 blockade triggers T cell-mediated destruction of immunogenic tumors. *Nat Med* 2015;21:1209–15.
38. Grasselly C, Denis M, Bourguignon A, Talhi N, Mathe D, Tourette A, et al. The antitumor activity of combinations of cytotoxic chemotherapy and immune checkpoint inhibitors is model-dependent. *Front Immunol* 2018;9:2100.
39. Gyori D, Lim EL, Grant FM, Spensberger D, Roychoudhuri R, Shuttleworth SJ, et al. Compensation between CSF1R+ macrophages and Foxp3+ Treg cells drives resistance to tumor immunotherapy. *JCI Insight* 2018;3:e120631.
40. Thommen DS, Schreiner J, Müller P, Herzig P, Roller A, Belousov A, et al. Progression of lung cancer is associated with increased dysfunction of T cells defined by coexpression of multiple inhibitory receptors. *Cancer Immunol Res* 2015;3:1344–55.
41. Zhang Y, Cai P, Liang T, Wang L, Hu L. TIM-3 is a potential prognostic marker for patients with solid tumors: a systematic review and meta-analysis. *Oncotarget* 2017;8:31705–13.
42. Komohara Y, Morita T, Annan DA, Horlad H, Ohnishi K, Yamada S, et al. The coordinated actions of TIM-3 on cancer and myeloid cells in the regulation of tumorigenicity and clinical prognosis in clear cell renal cell carcinomas. *Cancer Immunol Res* 2015;3:999–1007.
43. Tomkowicz B, Walsh E, Cotty A, Verona R, Sabins N, Kaplan F, et al. TIM-3 suppresses anti-CD3/CD28-induced TCR activation and IL-2 expression through the NFAT signaling pathway. *PLoS One* 2015;10:e0140694.
44. Xia Y, Shen S, Verma IM. NF-κB, an active player in human cancers. *Cancer Immunol Res* 2014;2:823–30.
45. Grasso CS, Giannakis M, Wells DK, Hamada T, Mu XJ, Quist M, et al. Genetic mechanisms of immune evasion in colorectal cancer. *Cancer Discov* 2018;8:730–49.
46. Garcia-Diaz A, Shin DS, Moreno BH, Saco J, Escuin-Ordinas H, Rodriguez GA, et al. Interferon receptor signaling pathways regulating PD-L1 and PD-L2 expression. *Cell Rep* 2017;19:1189–201.
47. Garcia M, Fernandez-Garcia NI, Rivas V, Carretero M, Escamez MJ, Gonzalez-Martin A, et al. Inhibition of xenografted human melanoma growth and prevention of metastasis development by dual antiangiogenic/antitumor activities of pigment epithelium-derived factor. *Cancer Res* 2004;64:5632–42.
48. Yang S, Lv Q, Luo T, Liu L, Gao R, Chen S, et al. Metformin inhibits expression and secretion of PEDF in adipocyte and hepatocyte via promoting AMPK phosphorylation. *Mediators Inflamm* 2013;2013:429207.
49. Dierge E, Debock E, Guilbaud C, Corbet C, Mignolet E, Mignard L, et al. Peroxidation of n-3 and n-6 polyunsaturated fatty acids in the acidic tumor environment leads to ferroptosis-mediated anticancer effects. *Cell Metab* 2021;33:1701–15.
50. Wu H, Han Y, Rodriguez Sillke Y, Deng H, Siddiqui S, Treese C, et al. Lipid droplet-dependent fatty acid metabolism controls the immune suppressive phenotype of tumor-associated macrophages. *EMBO Mol Med* 2019;11:e10698.